Minor elements in lead materials used for lead/acid batteries
1. Hydrogen- and oxygen-gassing characteristics

L.T. Lam*, J.D. Douglas, R. Pillig and D.A.J. Rand
CSIRO Division of Mineral Products, P.O. Box 124, Port Melbourne, Vic. 3207 (Australia)

Abstract

Minor elements are commonly present in the raw lead materials that are used to manufacture lead/acid batteries. Although certain of these elements are known to exert, individually, a marked influence on the gassing characteristics during charging, less is understood of their collective effects. As the first stage in an experimental campaign to obtain such information, the evolution of hydrogen and oxygen has been examined on both bare (grid) and doped/pasted electrodes. With the latter electrodes, different dopants (Ag, Bi, Cd, Cr, Ni, Sb, Se, Sn, Zn) have been introduced at a level of 0.1 wt.%. The subsequent gassing rates have been determined by application of either a potential-scan or a potential-step procedure. The latter has been conducted together with gas collection. The hydrogen-evolution characteristics on bare electrodes are dependent on the chosen lead alloy. The rate increases in the order: Pb < Pb–0.09Ca < Pb–0.07Bi < Pb–0.09Ca–0.4Sn < Pb–0.09Ca–0.3Sn < Pb–0.09Ca–0.7Sn < Pb–2.2Sb < Pb–1.7Sb < Pb–5.7Sb. By comparison, the oxygen-gassing rate does not exhibit such a clear relationship with alloy composition. In general, oxygen evolution above 1.7 V increases in the order: Pb < Pb–0.09Ca–0.3Sn < Pb–2.2Sb < Pb–0.09Ca ≈ Pb–5.7Sb < Pb–0.09Ca–0.7Sn < Pb–0.07Bi < Pb–0.09Ca–0.4Sn < Pb–1.7Sb. The Pb–0.09Ca–0.4Sn and Pb–1.7Sb electrodes exhibit abnormal hydrogen- and oxygen-evolution rates. This is probably due to the fact that these two alloys were made by a different manufacturer. The degree of hydrogen evolution on untreated and doped negative-material (pasted) electrodes can be classified in terms of a low, a medium, or a high rate. For elements that give a low rate, gassing increases in the order: Ag < Zn < untreated < Cd < Bi ≈ Cr. The Sn- and Se-doped electrodes exhibit a medium evolution rate. Finally, Sb- and Ni-doped electrodes display the highest rate of hydrogen evolution; of these, nickel exerts the stronger effect. All the dopants enhance oxygen evolution. The gassing rate increases in the order: untreated ≈ Cd < Se < Sn < Bi ≈ Cr < Ni ≈ Zn < Sb < Ag. The hydrogen- and oxygen-gassing behaviour of the doped electrodes is discussed in terms of the operating characteristics of valve-regulated batteries.

Introduction

Future specifications for automotive batteries will set increasingly lower water-consumption rates for flooded-electrolyte designs, and may even force the introduction of valve-regulated batteries (VRBs) based on absorbent glass-mat (AGM) technology. Although, at present, the latter batteries are used principally in duties that involve

*Author to whom correspondence should be addressed.

SSDI 0378-7753(93)01868-I

relatively shallow discharges (e.g., stand-by power supplies), the market shows a growing demand for VRBs in deep-cycling applications.

There have been several demonstrations [1–4] of the feasibility of VRBs for automotive service. It has been claimed that these batteries give competitive, or even better, results than flooded, low-maintenance designs [2, 3]. For example, the performance of VRBs is equivalent to that of flooded-electrolyte designs with low-antimony positive grids; but when both battery types use the same Pb–Ca–Sn alloy for the positive grids, the cycle-life and cold-cranking capabilities of VRBs are superior.

The principal factors that influence the cycle life of VRBs are the composition/nature of the grid alloys, the level of impurities in the starting lead materials employed for the positive and negative plates, and the charging conditions (i.e., constant current, or constant voltage with a limited current) [5–7]. These factors also affect directly the gassing behaviour of the battery. Minimization of the hydrogen- and oxygen-gassing rates, together with promotion of oxygen recombination, are important objectives in the design of such batteries. One approach is to use an AGM separator to immobilize the electrolyte and to facilitate oxygen recombination. The efficiency of recombination depends on the absorptivity and degree of electrolyte saturation of the glass mat. Overall, AGM separators must have high and well-defined porosity, rapid wicking, low electrical resistance, high compressibility, good stability against both acid and oxidative attack, and freedom from organic impurities.

In addition to the performance of the separator, inherent impurities in the starting lead materials are equally important because they can exert marked effects on the gassing rates of VRBs [5]. For further battery development, it is critical to determine the collective influence of such minor elements on gassing characteristics, as well as on deep-cycling performance. Such information will allow battery manufacturers to establish more accurately the level of purity required for the lead materials used in all types of lead/acid technology, i.e., low-maintenance, flooded-electrolyte and valve-regulated systems. Moreover, the studies may reveal that some of the minor elements are indeed advantageous.

Any impurity that depresses the hydrogen overvoltage with respect to pure lead is generally considered to be an anathema to VRBs. This view is held irrespective of whether the impurity originates from within the oxide, grid, electrolyte, or any other component of the battery. In practice, the folklore is not always true. Since the oxygen-recombination process that occurs at the negative plates in VRBs causes some decrease in the hydrogen-evolution rate, any impurity that promotes only a marginal increase in the rate above that for pure lead may be acceptable. For example, tin has a lower hydrogen overvoltage than either pure lead or lead–calcium alloys, but can be used effectively as an alloying agent for the grid metal.

The objective of this study is to determine the influence of minor elements, present in either the grid alloy or active material, on the hydrogen- and oxygen-gassing behaviour of lead/acid batteries. In the case of the positive and negative active materials, the chosen research strategy is to dope the starting leady oxide with the minor elements in their oxide forms.

Experimental

Electrode preparation

Bare (grid) electrodes

Pure-lead and lead-alloy grids were sectioned and a copper wire was soldered to one end of each sample. The resulting assemblies were then embedded, individually,

in epoxy resin to give cylindrical electrodes of diameter = 20 mm and height = 10 mm. After setting, the upper surface of each electrode was polished with abrasive papers of successively finer grade between 240 and 1200 grit. Final polishing was conducted on a series of cloths that were impregnated with alumina slurries of decreasing particle size, namely, 20, 5 and 1 μm.

Pasted electrodes

A section of a Pb–0.09Ca–0.4Sn grid* (i.e., the type used in the construction of VRBs) was embedded in epoxy resin to give a cylinder with the same dimensions as those of the bare-electrode assembly. The unsoldered end of the grid was allowed to protrude about 2 mm above the upper surface of the cylindrical mould (Fig. 1(a)). A polyvinyl chloride (PVC) rod with the same diameter as the assembly was sectioned into slices of thickness = 3 mm. A hole (diameter = 6 mm) was drilled through the centre of each slice and a cylindrical paper strip was fixed to the wall of the hole. The PVC slice was placed on the upper surface of the electrode assembly so that the grid was located at the centre of the hole (Fig. 1(a)). Untreated and doped pastes were prepared using the formulae given in Table 1. It should be noted that bismuth-free ball-mill oxide was used to produce the pasted electrodes. For doped material, the given element was added as an oxide powder to the leady oxide at a level of 0.1 wt.%. The resulting mixture was shaken in a container for 5 min prior to paste mixing. The hole in the above assembly was filled with paste and the PVC slice was then removed to give the final dimensions of the electrode, as shown in Fig. 1(b).

The pasted samples were cured to tribasic lead sulfate ($3PbO \cdot PbSO_4 \cdot H_2O = 3BS$). After curing, the samples were placed in a petri disc that contained 1.07 sp. gr. H_2SO_4. Electrode formation was achieved by applying, for 20 h, a constant current of 17.7 mA per g of cured material.

Gassing measurements

The electrochemical cell used in this study is shown in Fig. 2. The Pyrex cell has an H-shape; the two main compartments are joined by a glass frit. The electrolyte (1.275 sp. gr. H_2SO_4) was degassed with nitrogen for 30 min before introduction into

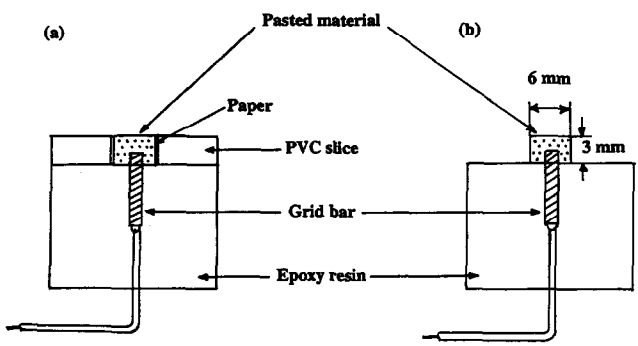

Fig. 1. Preparation of pasted electrodes for electrochemical studies.

*The number before each minor element represents the content, in wt.%, of that element in the alloy.

TABLE 1

Paste formulae for positive and negative electrodes

Component	Positive electrode	Negative electrod
Leady oxide (kg)	3	3
Fibre (g)	0.9	1.8
Carboxymethyl cellulose (g)	7.5	
Stearic acid (g)		1.8
$BaSO_4$ (g)		11.1
Vanisperse (g)		11.1
Carbon black (g)		6.3
H_2SO_4 1.40 sp. gr. (cm^3)	200	200
Water (cm^3)	390	330
Paste density (g cm^{-3})	4.5–4.6	4.7–4.8

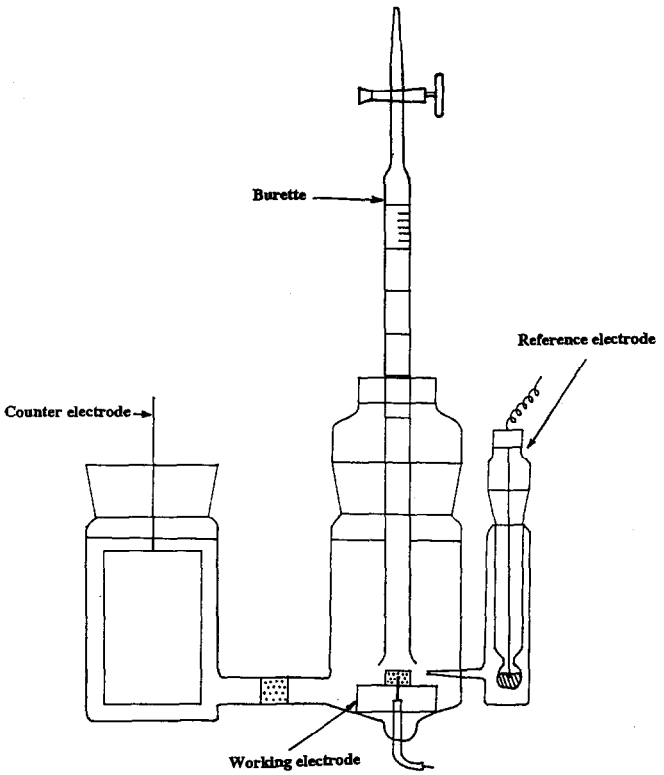

Fig. 2. Electrochemical cell used for gassing measurements.

the cell. The working electrode was either a bare grid or a plate-material sample, as prepared above. A sheet of pure lead served as the counter electrode. All potentials were measured (and are reported) with respect to a 5 M Hg/Hg_2SO_4 reference electrode in 1.275 sp. gr. H_2SO_4.

Bare (grid) electrodes

For hydrogen-gassing measurements, the potential of each sample was held initially at -1.3 V for approximately 30 min until the current dropped to a stable value. This treatment reduces any film of lead monoxide that is formed on the surface of the sample during standing in air, as well as any lead sulfate film that develops during immersion of the sample in the cell solution. The potential was then scanned from -1.3 to -1.7 V at 0.1 mV s^{-1} with a programmable potentiostat/galvanostat (EG&G PAR 273). The resulting voltammograms were displayed on an x–y recorder (Rikadenki RW-201). The amount of hydrogen evolved at each potential in the scan is represented by the current delivered.

Measurement of oxygen evolution at a given potential is complicated by the accompanying oxidation of the electrode substrate to lead dioxide. This necessitates the use of a potential-step procedure together with gas collection. The former involved stepping the potential of the sample to a given value and then holding for a given period. During this time, the potential, the total delivered current and the quantity of charge were recorded with a 3-pen recorder (YEW 3066). Simultaneously, the gas evolved was collected by solution displacement in a 25 ml burette that was located immediately above the sample. The oxygen-evolution current density, i_{O_2}, was calculated using the following relationship:

$$i_{O_2} = [4FV(P_{total} - P_w)]/[10^6 RTAt] \quad (1)$$

where: $F = 96\,500$ C mol^{-1}; P_{total} = total pressure in the upper part of burette (≈ 101.325 kPa); P_w = vapour pressure (kPa) at temperature T: V = gas volume (ml) collected in the burette; R = gas constant ($=8.31$ J mol^{-1} K^{-1}); T = absolute temperature; A = electrode area (cm^2); t = electrolysis period ($=3600$ s in this study).

Pasted electrodes

After formation, each sample was placed in the test cell and the potential was scanned, either between -1.1 and -1.7 V or between 1.3 and 1.7 V, at 5 mV s^{-1} for 20 cycles prior to the hydrogen/oxygen-gassing measurements. Over these potential ranges, any lead sulfate residues (due to incomplete formation and the chemical development of sulfation layers) will be converted, respectively, to lead or lead dioxide. For studies of both hydrogen and oxygen evolution, a potential-step technique was used and the gas produced at each potential was collected. The oxygen-evolution current density was determined from eqn. (1). The corresponding hydrogen-evolution current density, i_{H_2}, was calculated from the following expression:

$$i_{H_2} = [2FV(P_{total} - P_w)]/[10^6 RTAt] \quad (2)$$

Note, two or more separate determinations of the current were undertaken at each potential. The average values are reported.

Results and discussion

It is well known that during the charging of lead/acid batteries, the conversion of lead sulfate to either lead dioxide or lead will commence at the surface of the grid and then spread gradually out into the active material [8, 9]. In another words, the current concentrates on the grid during the initial stages of the charging process. Following increase in the battery voltage, the evolution of oxygen at the positives (and hydrogen at the negatives) will take place on the surfaces of both the active material

and the grid. Gassing will be more prominent on the grid if parts of the frame and wires are not covered with active material. This situation is commonly encountered when using a belt-pasting procedure. The paste generally covers one side (i.e., the upper) of the plate and leaves the grid frame and wires exposed on the side facing the belt. Therefore, an investigation has been made of the effects on gassing behaviour of bare grids produced from pure lead and different lead alloys.

Hydrogen evolution on bare (grid) electrodes

The rate of hydrogen evolution on bare pure-lead and lead-alloy electrodes is shown in Fig. 3. Based upon the electrocatalytic capability for hydrogen evolution, the grid-alloy electrodes can be classified into three main groups, namely: (I) Pb–Sb; (II) Pb–Ca–Sn; (III) pure lead, Pb–Ca and Pb–Bi.

The Pb–Sb alloys exhibit the highest electrocatalytic activity for hydrogen evolution. The rate is dependent upon the concentration of antimony and increases in the order: Pb–2.2Sb < Pb–1.7Sb < Pb–5.7Sb.

The electrodes in the second group, viz., the Pb–Ca–Sn alloys, display medium effects on hydrogen evolution. The rate increases in the order: Pb–0.09Ca–0.4Sn < Pb–0.09Ca–0.3Sn < Pb–0.09Ca–0.7Sn.

The group comprising pure lead, Pb–0.09Ca and Pb–0.07Bi exerts the least effect on the hydrogen-evolution rate. At a given potential, the hydrogen evolution on these electrodes increases in the order: Pb < Pb–0.09Ca < Pb–0.07Bi.

In the above results, the unexpected increase in the hydrogen-evolution rate of the Pb–Ca alloy with 0.3 wt.% Sn as opposed to that with 0.4 wt.% Sn, and the Pb–Sb alloy with 1.7 wt.% Sb as opposed to that with 2.2 wt.% Sb, may be due to different manufacturing conditions. The Pb–Ca–0.4Sn and Pb–1.7Sb alloys were produced by one manufacturer, and the remaining alloys in the Pb–Ca–Sn and Pb–Sb groups by another manufacturer. To understand further the observed difference in hydrogen-evolution rate, it should be noted that, in general, gassing reactions on metals are influenced by two factors:

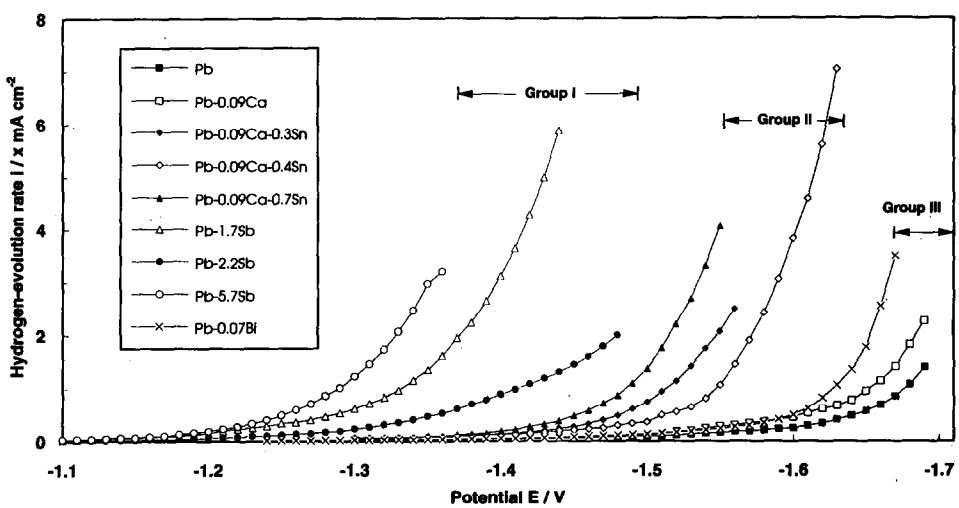

Fig. 3. Hydrogen-gassing rate on pure-lead and lead-alloy electrodes.

(i) the inherent characteristics of the metal itself; these exert differing degrees of interfacial dynamics on the charge-transfer level (for instance, the hydrogen-evolution potential is lower on nickel than on lead or mercury);

(ii) the 'effective' surface area of the metal; this is associated with the surface structure (grain size, grain boundary, etc.) and the surface morphology (roughness, defects, etc.), for example, hydrogen evolution is greater on platinum black than on smooth platinum metal. Different manufacturing conditions for the alloys will promote different surface structure/morphology and, therefore, will influence the rate of hydrogen gassing. Moreover, at the levels in the present alloys (i.e., 0.3 to 0.4 wt.% for Sn, 1.7 to 2.2 wt.% for Sb), the distribution of either tin or antimony is known to be sensitive to the grid-casting procedure. In particular, the casting conditions can affect the degree of segregation of the constituent elements in the grain boundaries of the alloys.

The Tafel plots (i.e., potential versus log i) of the above performance curves are given in Fig. 4. Except for Pb–Sb alloys, the Tafel plots exhibit an inflection that separates the data into two distinct linear relationships: one at low potentials, the other at high potentials. A similar phenomenon has been observed by Papageorgiou *et al.* [10]. By contrast, the current for Pb–Sb alloys increases monotonically over the entire potential range. It should be pointed out, however, that the hydrogen-evolution rate and the corresponding Tafel slope will be strongly affected by any change in the structure of the electrode double-layer that results either from the adsorption of organic impurities [11] or from the formation of an oxide film on the lead surface [12]. Therefore, for those curves that exhibit an inflection, only the electrochemical parameters associated with the high-potential range have been calculated from the following Tafel relationship for potential, E, and current density, i:

$$E - E_{eq} = \eta = a + b \log i \tag{3}$$

where E_{eq} is the equilibrium potential under zero-current conditions; η is the over-potential. The parameters a (the intersection point at $\log i = 0$) and b (the 'Tafel

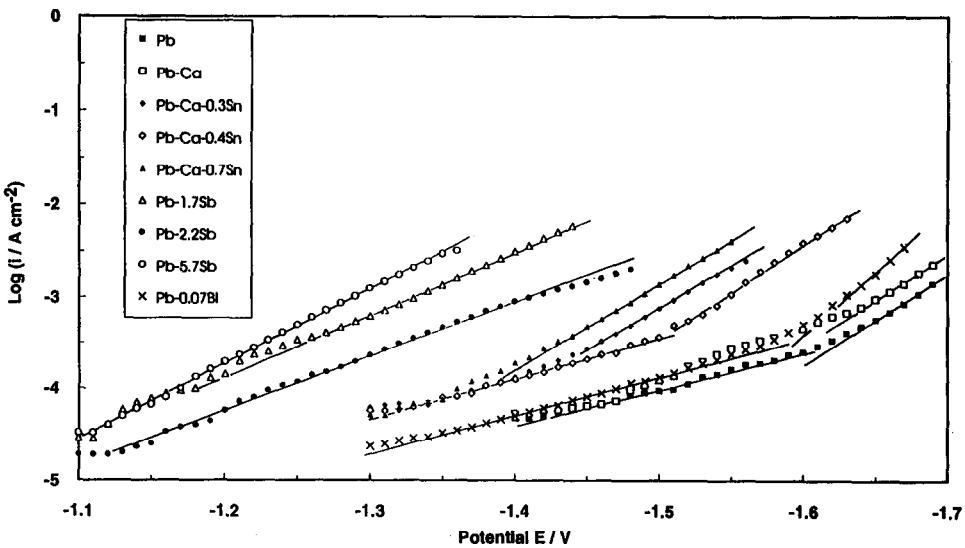

Fig. 4. Tafel plots for hydrogen evolution on pure-lead and lead-alloy electrodes.

slope') are given by:

$$a = 2.303RT/\beta nF \log i_0 \quad (4)$$

$$b = 2.303RT/\beta nF \quad (5)$$

and the logarithm of the exchange current density (log i_0) is given by:

$$\log i_0 = a/b \quad (6)$$

In eqns. (4) to (6): n = number of moles of electrons involved in the reaction ($n = 1$ for hydrogen-evolution reaction); β = symmetry factor; $\alpha = (1 - \beta)$ = transfer coefficient; i_0 = exchange-current density (A cm^{-2}). The parameters F, R and T are the same as those defined above for eqn. (1).

The Tafel slope, b, and the exchange-current density, i_0, are usually taken to characterize the kinetics of the hydrogen-evolution reaction. The measurement of the exchange-current density provides a general idea of the reaction rate in the standard equilibrium state and, thereby, permits classification of the substrate upon which the reaction is occurring as either a good or a bad electrocatalyst for hydrogen evolution. That is, the lower the exchange-current density, the poorer the electrocatalyst, and vice versa. The Tafel slope (or transfer coefficient) is a useful indication of the reaction mechanism, but usually requires certain assumptions.

Inspection of the exchange-current densities (Table 2) shows that the electrocatalytic activity for hydrogen evolution increases in the order: Pb ≈ Pb–Ca ≈ Pb–Bi < Pb–Ca–Sn alloys < Pb–Sb alloys. This finding is in general agreement with the conclusions reached above from cyclic voltammetric studies.

Oxygen evolution on bare (grid) electrodes

The oxygen-evolution characteristics of pure lead and lead-alloys are presented in Fig. 5. Unlike the results obtained for hydrogen, the rate of oxygen evolution does not display a clear relationship with the alloy type. Again, the Pb–0.09Ca–0.4Sn and Pb–1.7Sb alloys exhibit abnormal behaviour, namely, the oxygen-evolution rate is higher on these electrodes than on either pure lead or the other alloys. As suggested above,

TABLE 2

Electrochemical parameters for the hydrogen-evolution reaction on pure lead and lead alloys

Electrode	Tafel slope, b (V)	Log (i_0/A cm^{-2})
Group III		
Pb	−0.102	−13.18
Pb–0.09Ca	−0.101	−12.77
Pb–0.07Bi	−0.096	−12.90
Group II		
Pb–0.09Ca–0.3Sn	−0.109	−10.71
Pb–0.09Ca–0.4Sn	−0.094	−12.19
Pb–0.09Ca–0.7Sn	−0.109	−10.43
Group I		
Pb–1.7Sb	−0.147	−7.37
Pb–2.2Sb	−0.167	−7.43
Pb–5.7Sb	−0.123	−8.03

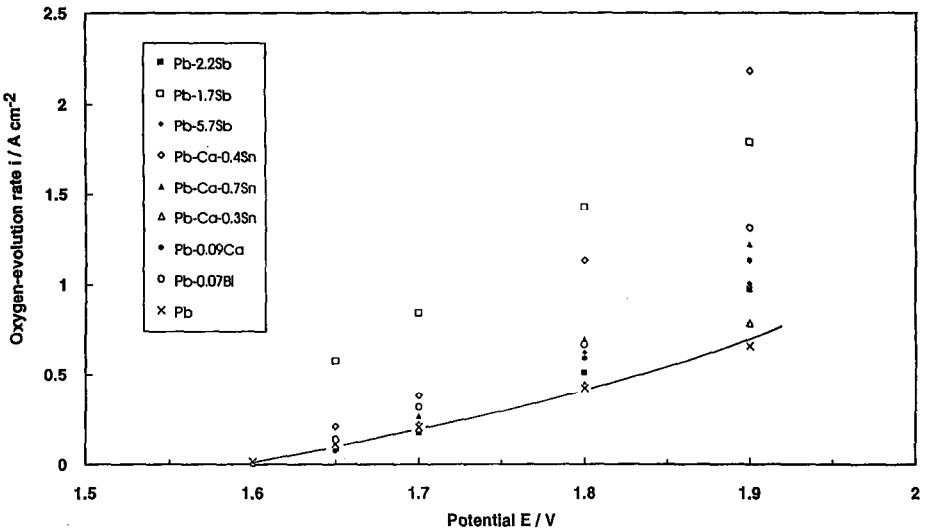

Fig. 5. Oxygen evolution on pure-lead and lead-alloy electrodes.

this may due to a dissimilarity in the manufacturing practice that has been employed by the two suppliers. For the remaining alloys, at potentials below 1.7 V, there is little difference in the oxygen-evolution rate; Pb–0.09Ca has the lowest oxygen-evolution rate. At 1.7 V, oxygen evolution increases in the order: Pb ≈ Pb–0.09Ca ≈ Pb–0.09Ca–0.3Sn ≈ Pb–2.2Sb ≈ Pb–5.7Sb < Pb–0.09Ca–0.7Sn < Pb–0.07Bi.

At potentials above 1.7 V, the order becomes: Pb < Pb–0.09Ca–0.3Sn < Pb–2.2Sb < Pb–0.09Ca ≈ Pb–5.7Sb < Pb–0.09Ca–0.7Sn < Pb–0.07Bi.

Hydrogen evolution on pasted electrodes

Hydrogen-evolution data for untreated and doped negative plates are shown in Fig. 6. As expected, Ni- and Sb-doped samples exhibit the highest hydrogen-evolution rate compared with untreated and other doped samples. The Ag- and Zn-doped electrodes display the lowest activity for hydrogen evolution. In summary, the effect of dopants on hydrogen evolution increases in the order: Ag < Zn < untreated < Cd < Bi ≈ Cr < Sn ≈ Se < Sb < Ni.

The rate of hydrogen evolution is governed largely by the concentration of metal oxide impurities that can be deposited on the negative electrode and by the ability of these impurities to sustain a lower hydrogen overpotential than lead. The situation with chromium requires some explanation. It is observed that the rate of hydrogen evolution is low with chromium, despite the fact that this metal is known to have a low hydrogen overpotential. The deposition of chromium is complicated [13]. First, a passive film composed of $[Cr_2(CrO_4)](SO_4)_2$ is formed on the surface of the cathode from the mixture of CrO_3 and sulfuric acid solution. Second, the reduction of Cr^{3+} to Cr^0 takes place when the concentration of Cr^{3+} is increased to a certain value (≈ 0.3 wt.%). Since, in the studies reported here, CrO_3 was added to leady oxide at a level of 0.1 wt.%, metal chromium could not be deposited on the negative material and this would explain the absence of any major effect on the hydrogen-gassing characteristics.

The Tafel plots for the above hydrogen-gassing curves are given in Fig. 7. Each plot exhibits good linearity. The corresponding slope and the logarithm of the exchange-

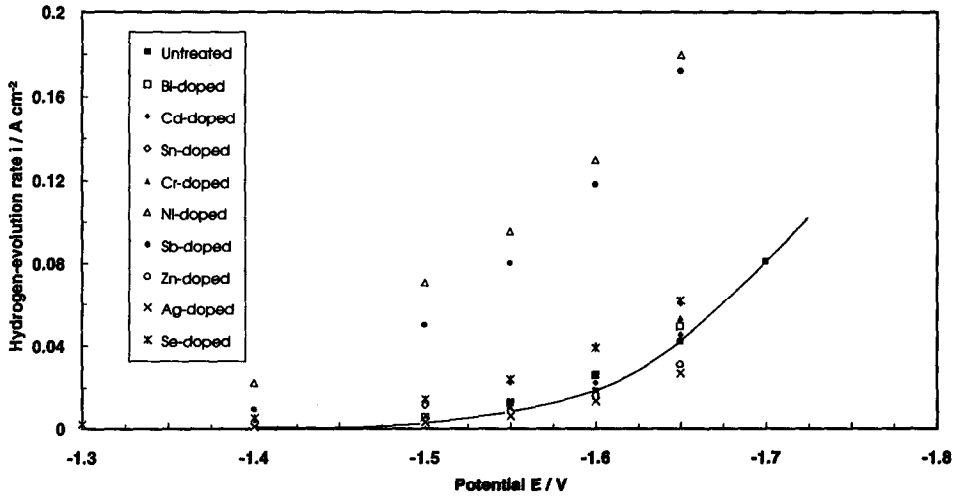

Fig. 6. Hydrogen evolution on untreated and doped/pasted electrodes.

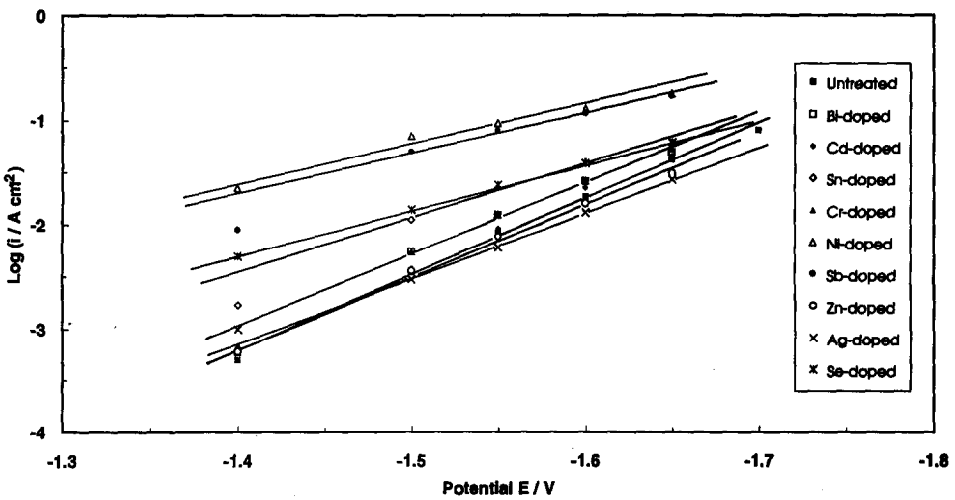

Fig. 7. Tafel plots for hydrogen evolution on untreated and doped/pasted electrodes.

current density for each dopant are listed in Table 3. From the magnitude of the exchange-current density, the effect of the dopants on the hydrogen-evolution rate can be classified into three groups: (i) low hydrogen-evolution rate: untreated and doped electrodes containing Ag, Zn, Cd, Bi or Cr; (ii) medium hydrogen-evolution rate: Sn- and Se-doped electrodes; (iii) high hydrogen-evolution rate: Sb- and Ni-doped electrodes. It should be pointed out, however, that it is difficult to use the exchange-current density to define further the influence of the various dopants within the same group. This is because the resulting differences in rate are small, as can be seen from the respective voltammograms (see Fig. 6).

TABLE 3

Electrochemical data for hydrogen evolution on pasted electrodes

Electrode/dopant	Tafel slope, b (V)	Log (i_0/(A cm^{-2})
Low rate		
Untreated	−0.133	−8.83
Ag	−0.150	−8.13
Zn	−0.142	−8.30
Cd	−0.132	−8.70
Bi	−0.130	−8.81
Cr	−0.130	−8.81
Medium rate		
Sn	−0.186	−6.40
Se	−0.209	−6.00
High rate		
Sb	−0.246	−4.68
Ni	−0.260	−4.43

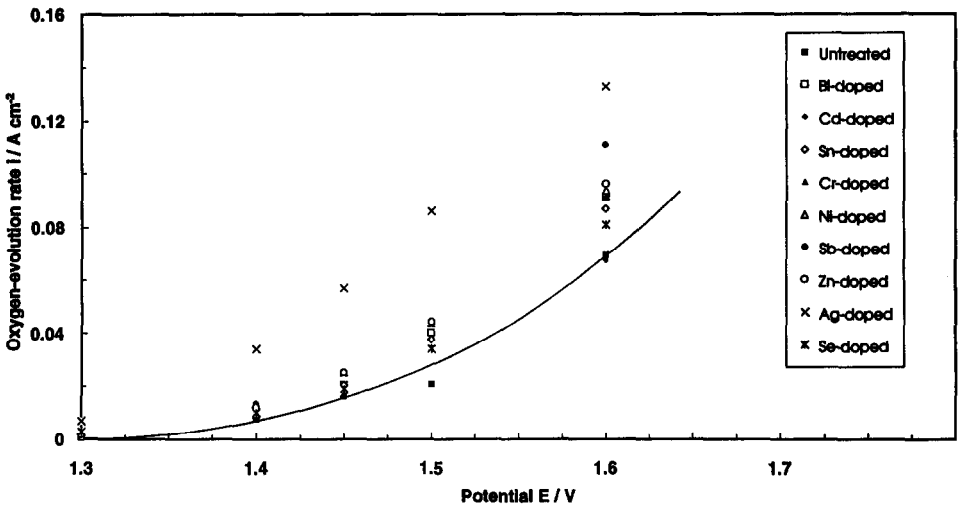

Fig. 8. Oxygen evolution on untreated and doped/pasted electrodes.

Oxygen evolution on pasted electrodes

Figure 8 presents the rate of oxygen evolution on different pasted electrodes. Overall, the effect of the dopants on oxygen evolution at potentials above 1.5 V increases in the order: untreated ≈ Cd < Se < Sn < Bi ≈ Cr < Ni ≈ Zn < Sb < Ag. At potentials below 1.5 V, there are only minor differences in the oxygen-evolution rate on Sn-, Bi-, Se- and Cr-doped electrodes.

Relevance to valve-regulated batteries

During the overcharge of flooded-electrolyte batteries, the potentials of the positive and negative plates shift away from the respective equilibrium values by approximately

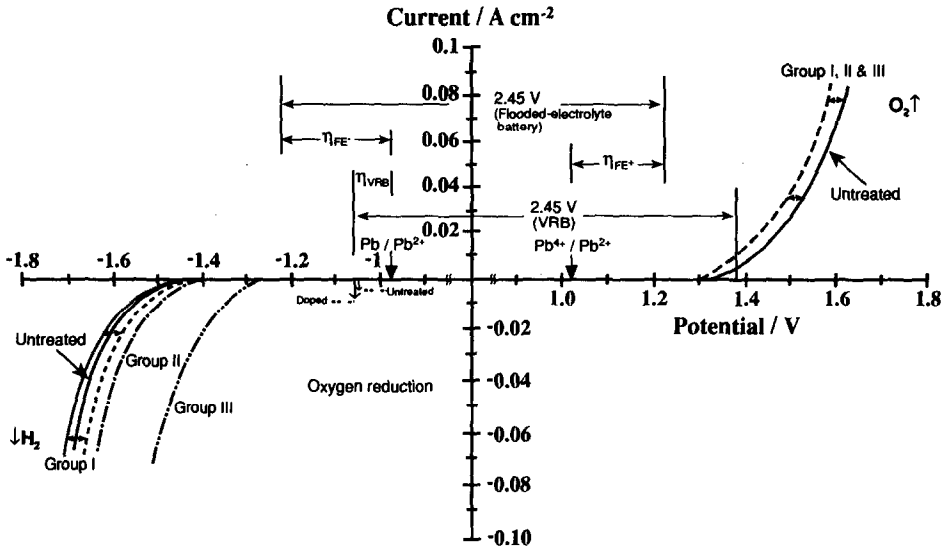

Fig. 9. Operational potential of a valve-regulated battery.

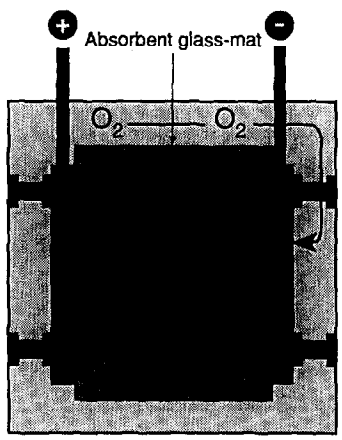

Fig. 10. Schematic of oxygen recombination in a valve-regulated battery.

the same amounts (η_{FE}, see Fig. 9). In VRBs, the overcharge current forces the transport of oxygen through either the pores of the separator or the head space of the container, as shown in Fig. 10. At a typical upper limit for the charging voltage of 2.45 V/cell, the oxygen produced at the positive plate is reduced at the negative plate via the formation of lead sulfate, i.e.:

$$2Pb + O_2 + 2H_2SO_4 \longrightarrow 2PbSO_4 + 2H_2O \quad (7)$$

$$2PbSO_4 + 4H^+ + 4e^- \longrightarrow 2Pb + 2H_2SO_4 \quad (8)$$

Overall:

$$O_2 + 4H^+ + 4e^- \longrightarrow 2H_2O \quad (9)$$

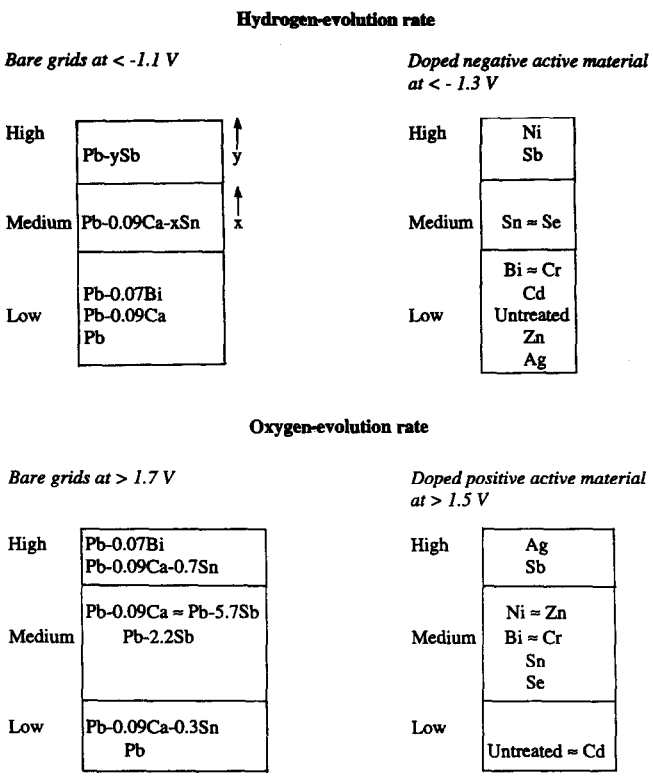

Fig. 11. Summary of effect (low to high) of grid-alloy composition and dopants on hydrogen-/oxygen-gassing rates; Pb–0.09Ca–0.4Sn and Pb–1.7Sb are excluded.

The oxygen-recombination reaction maintains the negative plate in a partially discharged state and, as a result, the potential is kept near the equilibrium value for the $Pb/PbSO_4$ system (i.e., $\eta_{VRB} = \approx 80$ mV [14], Fig. 9). At this potential, there will be a marked reduction in the hydrogen-gassing rates of both the untreated and doped electrodes. Furthermore, from the relative behaviour of the electrodes at more negative potentials, it can be concluded that, during charging of VRBs, hydrogen evolution will be lowest with Group I dopants (i.e., Ag, Zn, untreated, Cd, Bi and Cr, see Fig. 6 and Table 3). At positive plates, each doped electrode exhibits a higher oxygen-evolution rate than that experienced on the untreated counterpart. The spread of the effect is, however, less than that observed for hydrogen evolution. Moreover, since the diffusion of oxygen to the negative and the subsequent rate of reduction to water are both proportional to the oxygen-partial pressure [15–17], a higher rate of oxygen evolution may be beneficial for oxygen recombination.

Conclusions

An examination has been made of the gassing properties of hydrogen and oxygen on pure-lead, lead alloy and pasted electrodes that have been prepared with/without different dopants. The studies have provided an essential benchmark for the exploration of synergistic effects between the various dopants. From the results obtained, the following conclusions can be drawn.

1. The hydrogen-evolution rate on bare (grid) electrodes increases in the order: Pb < Pb–0.09Ca < Pb–0.07Bi < Pb–0.09Ca–0.4Sn < Pb–0.09Ca–0.3Sn < Pb–0.09Ca–0.7Sn < Pb–2.2Sb < Pb–1.7Sb < Pb–5.7Sb.

2. The dependence of the oxygen-evolution rate on electrode composition is less distinct but, in general, increases in the general order: Pb < Pb–0.09Ca–0.3Sn < Pb–2.2Sb < Pb–0.09Ca ≈ Pb–5.7Sb < Pb–0.09Ca–0.7Sn < Pb–0.07Bi < Pb–0.09Ca–0.4Sn < Pb–1.7Sb.

3. The manufacturing conditions of the lead alloy can exert a marked effect on the rate of hydrogen and oxygen evolution. Pb–0.09Ca–0.4Sn and Pb–1.7Sb give higher gassing rates than Pb–0.09Ca–0.3Sn and Pb–2.2Sb alloys. The two respective pairs of alloys have been produced by different battery manufacturers.

4. The addition of dopants to the negative material causes an increase in the hydrogen-gassing rate in the order: Ag < Zn < untreated < Cd < Bi ≈ Cr < Sn ≈ Se < Sb < Ni. The Ag- and Zn-doped electrodes suppress the normal evolution rate of hydrogen on negative electrodes.

5. All the dopants examined to date in this study yield a higher oxygen-evolution rate than the untreated variety. This effect increases in the order: untreated ≈ Cd < Se < Sn < Bi ≈ Cr < Ni ≈ Zn < Sb < Ag.

To assist the comprehension of the data presented here, the effects of grid-alloy composition and dopants on the hydrogen- and oxygen-gassing rates are presented schematically in Fig. 11.

Acknowledgements

The authors are grateful to Pasminco Limited for supporting this work and for permission to publish the results. Thanks are also due to Mr J.E. Manders of Pasminco Limited for his encouragement and helpful discussions.

References

1 B. Culpin, K. Peters and N.R. Young, in J. Thompson (ed.), *Power Sources 9, Research and Development in Non-Mechanical Electrical Power Sources*, Academic Press, London, 1983, p. 129.
2 E. Nann, *J. Power Sources, 33* (1991) 93.
3 M. Tsubota, S. Osumi and M. Kosai, *J. Power Sources, 33* (1991) 105.
4 T. Yamada, Y. Nakazawa and Y. Tsujino, *J. Power Sources, 38* (1992) 123.
5 J. Szymborski and B. Burrows, in J. Thompson (ed.), *Power Sources 9, Research and Development in Non-Mechanical Electrical Power Sources*, Academic Press, London, 1983, p. 113.
6 B. Culpin, M.W. Pilling and F.A. Fleming, *J. Power Sources, 24* (1988) 127.
7 J. Kwasnik, T. Pukacka, M. Paszkiewicz and B. Szczesniak, *J. Power Sources, 31* (1990) 135.
8 D. Pavlov, G. Papazov and V. Iliev, *J. Electrochem. Soc., 119* (1972) 8.
9 L.T. Lam, A.M. Vecchio-Sadus, H. Ozgun and D.A.J. Rand, *J. Power Sources, 38* (1992) 87.
10 N. Papageorgiou and M. Skyllas-Kazacos, *Electrochim. Acta, 37* (1992) 269.
11 J.O.M. Bockris and S. Srinivasan, *Electrochim. Acta, 9* (1964) 31.
12 D.G. Ives and F.R. Smith, *Trans. Faraday Soc., 62* (1967) 217.
13 N.E. Ryan, *Met. Finishing*, (Jan.) (1965) 46.
14 J.A. Magyar, M.A. Kepros and R.F. Nelson, *J. Power Sources, 31* (1990) 93.
15 N.D. Hung, J. Garche and K. Wiesener, *Tap Chi Hoat Dong Khoa Hoc, 26* (1988) 8.
16 N.D. Hung, J. Garche and K. Wiesener, *Tap Chi Hoat Dong Khoa Hoc, 27* (1989) 1.
17 H. Dietz, M. Radwan, J. Garche, H. Döring and K. Wiesener, *J. Appl. Electrochem., 21* (1991) 221.